Multivariate Analysis and Warning of a Tornado Embedded in Tropical Cyclone in Southern China

Zhaoming Li, Haonan Chen, *Senior Member, IEEE*, Hongxing Chu, Haobo Tan, V. Chandrasekar, *Fellow, IEEE*, Xianxiang Huang, and Shuofu Wang

***Abstract*—An EF1 tornado associated with tropical cyclone (TC) Ewiniar hit Dali Town, Foshan, Guangdong Province at 06:03 UTC on June 8, 2018, and the first special tornado warning was issued to five towns at 05:05 UTC. This article utilizes minute-scale observations from an X-band dual-polarization radar and measurements from an S-band Doppler radar to resolve the polarization characteristics associated with this tornado. In addition, second-scale atmospheric pressure data obtained from micropressure gauge and NCEP FNL (Final) Operational Global Analysis data are used to investigate the synoptic conditions and features of gravity waves (GWs). The conspicuous features of the descending reflectivity core, Doppler velocity couplet, Z_{DR} arc, K_{DP} foot, and the separation of the Z_{DR} arc and K_{DP} foot are detailed to quantify the tornadic evolution. The amplitude fluctuation of the GWs suddenly increased to 77.3 Pa, 2 h before the tornado occurred. Two focus regions with K_{DP} values greater than 6°/km are discussed by combining the Doppler velocity couplet and Z_{DR} arc. The separation distance of the Z_{DR} arc and K_{DP} foot was approximately 2.1 km. The appearance of these features may be indicative of fundamental processes intrinsic to tornado storms.**

***Index Terms*—Polarimetric weather radar, severe weather, tornado warning.**

I. Introduction

TORNADOES are one of the most violent weather phenomena and are always accompanied by strong convective weather, such as hail, heavy rain, and thunderstorms. On a global scale, the annual average number of tornadoes can exceed 1000 in the United States [1]; the annual average number of tornadoes in Europe has been 483 in recent years with a clear increasing trend [2]. The total number of significant tornadoes in China was 165 from 1961 to 2010, most of which occurred in plain areas, including areas in South China, the Northeast China Plain, the Jianghuai Plain, and the North China Plain [3].

An initial study of tornadic environments began in the late 1940s by Miller and Fawbush and included a detailed analysis of the environment on subsynaptic scales. In the early 1950s, the Weather Bureau Army Navy in the United States established a convective forecasting group to issue tornado warnings. Mesoscale analysis of tornadoes was originally accomplished by Fujita [4], and then the schematic evolution of the hook echo and the concept of mesocyclones combining original radar film and surface observations from available stations were developed [5]. Tornadic storms and airflows in tornadic storms have been systematically examined using radar as the primary observational tool. The dome characteristics in thunderstorms correspond to strong continuous updrafts [6], [7]. During the 1970s, Burgess and Brown [8] found that the Doppler velocity signature of the presence of maximum positive and negative velocities in adjacent azimuths coincides with the location of the tornado touchdown by analyzing several tornado cases. The tornadic vortex signature (TVS) was proposed to describe this characteristic, which first appears in the middle layer of thunderstorms, enhances at every height, and then touches the ground to form a tornado [9]–[11]. In the fall of 1990, the first Weather Surveillance Radar-1988 Doppler (WSR-88D) instrument was installed in Norman, Oklahoma, with the purpose of identifying tornadoes using the TVS. Tornado warnings improved significantly after the deployment of the WSR-88D network: The percentage of tornado warnings increased from 35% to 60%, and the mean lead time of tornado warnings increased from 5.3 to 9.5 min. More importantly, the expected fatalities and injuries were reduced by 45% and 40%, respectively, during tornado events. The Verification of the Origins of Rotation in Tornadoes Experiment (VORTEX) was successively implemented between 1994–1995 and 2009–2010 to explore tornado genesis and structures and improve forecasts. The VORTEX also provided us with further understanding of the thermal and dynamic structures of hook echoes and areas of rear flank downdraft [12]–[14].

Nevertheless, very few meteorological instruments are good at observing the fine structures of fast-evolving, small-scale, and short-lived tornadoes. Dual-polarization radars can provide both vertical and horizontal information about the features of scattering particles in the resolution volume. In addition to the conventional variables of reflectivity factor at horizontal polarization (Z_h), Doppler velocity (V), and Doppler spectrum width (SW), the new variables are the differential reflectivity

Manuscript received May 30, 2021; revised September 24, 2021 and October 15, 2021; accepted October 30, 2021. Date of publication November 4, 2021; date of current version November 22, 2021. This work was supported in part by the Radar Application and Short-term Severe-weather Predictions and Warnings Technology Program of Guangdong Meteorological Service under Grant GRMCTD202002, and in part by Academician Workstation in Foshan Meteorological Service under Grant 2021002. The work of Haonan Chen and V. Chandrasekar was supported by Colorado State University. *(Corresponding author: Haonan Chen.)*

Zhaoming Li, Hongxing Chu, Haobo Tan, Xianxiang Huang, and Shuofu Wang are with the Foshan Meteorological Service/Foshan Tornado Research Center, Foshan 528000, China (e-mail: lizhaoming@mail.iap.ac.cn; chuhongxing52@163.com; hbtan@grmc.gov.cn; fsqxj@163.com; shuofuwang@163.com).

Haonan Chen and V. Chandrasekar are with the Department of Electrical and Computer Engineering, Colorado State University, Fort Collins, CO 80523 USA (e-mail: haonan.chen@colostate.edu; chandra@colostate.edu).

Digital Object Identifier 10.1109/JSTARS.2021.3125269

This work is licensed under a Creative Commons Attribution 4.0 License. For more information, see https://creativecommons.org/licenses/by/4.0/

(Z_{DR}), meaning the logarithmic ratio of the reflectivity factors at *H* and *V* polarization, differential propagation phase shift (ϕ_{DP}), resulting difference in phase shift between *H* and *V* polarization, specific differential phase (K_{DP}), the amount of differential phase shift per unit distance, and the co-polar correlation coefficient (ρ_{HV}). The size, shape, composition, and orientation of scattering particles from dual-polarization radars reflect different types of hydrometeors and can be used to demonstrate the characteristics of tornadoes. A descending reflectivity core (DRC) may appear at the beginning of the tornado and can be a signature used to detect tornado genesis. The definition of DRCs and a preliminary survey in supercell storms were described by Rasmussen [15] after analyzing limited examples, which puts forward the hypotheses that flow stagnation or growing cumulus tower merges and creates a confined region where precipitation develops rapidly and descends into the periphery of the main updraft. A statistical survey of 64 isolated supercells with persistent rear-flank hook echo appendages indicated that DRCs have no necessary relationship with tornadoes [16]. Three types of DRCs were categorized based on different precipitation observations by Doppler on Wheels radars [17]. The tornadic debris signature (TDS) was first reported by Ryzhkov *et al.* [18]. Based on the tornado case outbreaking on May 3, 1999 in Oklahoma, anomalously low ρ_{HV} and Z_{DR} values of approximately zero were identified as features of the TDS. More tornado cases were analyzed to quantify the polarimetric radar variables as low values of ρ_{HV} less than 0.5, low values of Z_{DR} less than 0.5 dB, and high values of Z_h greater than 45 dBZ [19]. Bluestein *et al.* [20] used finer spatial resolution data from dual-polarization X-band mobile radar to investigate debris rings in tornadoes and showed that debris rings demonstrated Z_{DR} values less than 0.5 dB, ρ_{HV} values less than 0.5, and a large range of Z_h values. The polarimetric analysis of supercells at low levels conducted by Kumjian and Ryzhkov [21] found that, in a region of enhanced Z_{DR} along the inflow side of the forward flank referred to as the "Z_{DR} arc," the simultaneous appearance of an enhanced region of K_{DP} noted as the "K_{DP} foot" occurred, as described by Romine [22]. These phenomena were indicative of a kinematic property of supercell storms. Differences in observations between S-band and X-band radar during tornadic supercells summarized by Snyder *et al.* [23] revealed that the Z_{DR} arc emerges along the inflow side of the forward-flank downdraft (FFD), representing size sorting, as mentioned by Kumjian and Ryzhkov [21]. These separated horizontal scale features on radar displays occur due to sorting of drops based on size because smaller drops take longer to fall through a layer than larger drops do, and this residence time allows smaller drops to advect farther downstream by the storm-relative winds than larger drops. This generates horizontal-scale separation between larger and smaller drops corresponding to the separation of enhanced low-level regions of Z_{DR} and K_{DP} in supercells [24], which may be an intriguing signal for producing tornadoes. Many recent studies have started to exploit the relationship between these two regions' separation features in supercells and nonsupercells as well as tornadic and nontornadic cases [25]–[27]. Loeffler *et al.* [28] considered both the magnitudes and the orientations of the shifts between the two regions and found that tornadic supercells have orientations more orthogonal to the storm motion than do nontornadic supercells. The relationships between the hook echo, weak echo hole, weak echo column, and rotational couplet with visual tornadic characteristics were initially presented with photogrammetry by Wakimoto *et al.* [29]. Previous studies of tornadoes in China have mainly focused on different (regional) tornado climate, including tropical cyclone (TC) tornadoes [30]–[32], midlatitude tornadoes [33], and tornadoes formed in a typical environment of midlevel large-scale cold vortex [34]. The environmental conditions, radar echo structures and Doppler wind analyses, as well as associated damage survey were the key considerations in those studies [35], [36].

Aimed at monitoring small-scale strong convective weather such as tornadoes, an X-band radar network composed of four polarimetric radars was deployed in Foshan, Guangdong Province. An EF1 tornado associated with TC Ewiniar hit Dali Town, Foshan, at 06:03 UTC on June 8, 2018. The tornado path was narrow and long with a length of approximately 350 m and a width of less than 100 m. The damage area was mainly concentrated in the yellow frame area of A and B in the Bomei aluminum hardware city, Dali Town, shown in Fig. 1. The tornado was first seen in area A, as indicated by eyewitnesses E1 and E2, where light objects such as asbestos tiles were rolled up, and parts of roofs were lifted. The most damaged area was the yellow B region shown in Fig. 1, where a steel-frame roof was rolled up and fell to the ground. The metal sheet was scattered around, and some of it was rolled up and scattered a few hundred meters away. The damaged roof before and after the tornado is depicted in Fig. 1, which was observed by eyewitnesses E3 and E4. The video evidence was taken by C1 using a cell phone, and the shooting direction was along the green arrow. The video shows that some iron pieces rolled up by the tornado were spinning in the air.

The tornadic storm was captured by one of the Foshan X-band dual-polarization radar nodes that is located approximately 13 km from Dali Town. As such, this study takes advantage of using high-resolution X-band dual-polarization radar to monitor tornadoes and resolve tornadic signatures [37]–[40]. This is among the first studies of such kind in China. Based on our analysis, the first specific tornado warning (in China) was successfully issued 58 min in advance. In fact, very few studies have reported the DRCs of tornadic storms at such close ranges from the radar, and the periodic-amplitude dynamic-spectral variation characteristics of GWs caused by tornadic storms have never been investigated in the literature.

The minute-scale measurements from the polarimetric X-band radar, 6-min volume data from a nearby S-band Doppler radar, second-scale atmospheric press data from micropressure gauge, and NCEP FNL (Final) Operational Global Analysis $1.0^\circ \times 1.0^\circ$ data were utilized to resolve the radar characteristics and gravity wave (GW) features of this typhoon-peripheral EF1 tornado. The rest of this article is organized as follows. Section II describes the data and methods used in this study. The synoptic conditions are detailed in Section III. Section IV

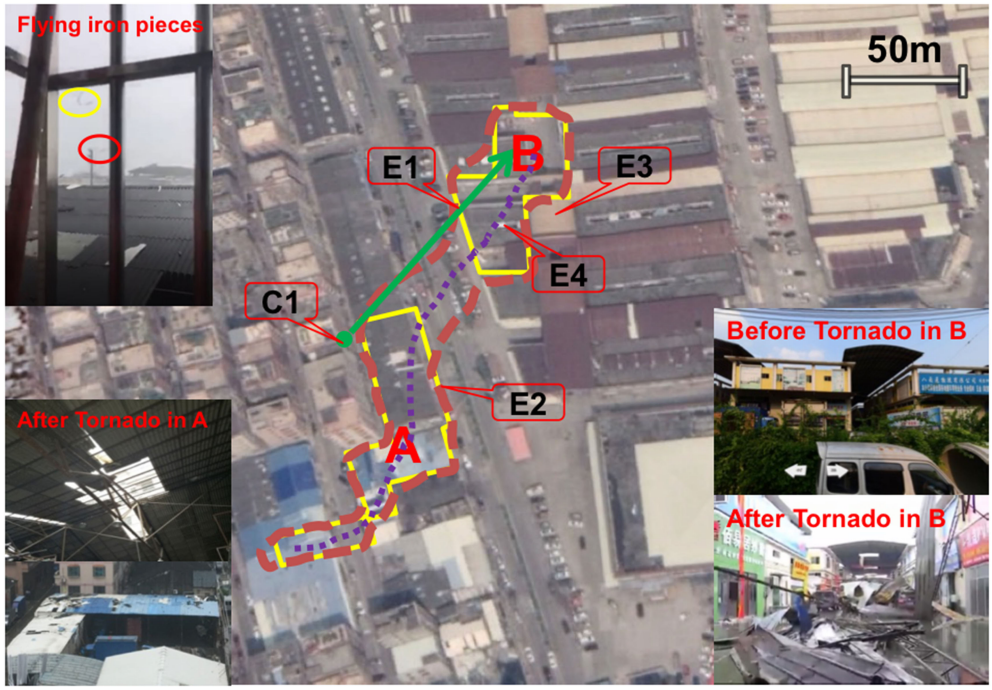

Fig. 1. Tornado path (purple dashed line), damage area (red dashed line, mainly in A and B), and the locations of the eyewitnesses (E1,..., E4) and photographer (C1) during this tornado event.

introduces the characteristics and evolving features of this tornado through multivariate analyses. A summary is provided in Section V.

II. Data and Methodology

During this event, many types of monitoring devices managed and operated by the Foshan Meteorological Service were active, including X-band dual-polarization radar, S-band Doppler radar, and micropressure gauges. Data with high temporal–spatial resolutions obtained from these devices were utilized to address the polarization characteristics and GW features of the tornado. The main specifications of the X-band dual-polarization radar and the S-band Doppler radar are listed in Table I. The TC best track (obtained from tcdata.typhoon.org.cn) [41], [42] and locations of monitoring devices are illustrated in Fig. 2. The blue and green solid points indicate the TC track at different stages: The blue solid points are the tropical storm (TS) stage, whereas the green solid points are the tropical depression (TD) stage. The S-band Doppler radar has a coverage range of 230 km, and the X-band dual-polarization radar has a coverage range of 75 km. The red dots represent the locations of the micropressure gauges. The inverted triangle indicates the tornado touchdown, which occurred during the TS stage at a distance of 75 km from the TS location at 06:00 UTC on June 8.

The X-band radar provided fine-scale observations during the prescribed tornado event, including seven parameters at each range volume, including Z_h, V, SW, Z_{DR}, ρ_{HV}, ϕ_{DP}, and K_{DP}. To fully capture small- to medium-scale severe weather systems with short life cycles and supply minute-scale observations, the X-band dual-polarization radar was set up in the fast volume coverage pattern (VCP) mode, which only includes scans at two low-level elevation angles, i.e., 1.8° and 2.8°.

TABLE I
Main Specifications of the X-Band Dual-Polarization and S-Band Doppler Radars Used in This Study

Radar specifications	X-band	S-band
Transmitter	Klystron	Klystron
Antenna Size (m)	2.4	8.5
Beam Width (°)	0.97	0.93
Antenna Gain(dB)	44.3	45.2
Polarization	STSR	Single Polarization
Transmit Frequency (MHz)	9350	2885
Transmit Peak Power (Kw)	75	650
Pulse Width (μs)	0.5	6.67
PRF (Hz)	300∼2000	322∼1304
Radial Resolution (m)	75	1000
Minimum Discernible Signal (dBm)	107	109
Receiver Dynamic Range (dB)	85	85
Observation parameters	Z_h, V, SW Z_{DR}, ϕ_{DP} K_{DP}, ρ_{HV}	Z_h, V, SW

Similar to WSR-88D from both hardware and software perspectives, the S-band Doppler radar used in this study was routinely operating in VCP21 mode during this tornado event, providing surveillance scans at nine elevation angles, i.e., 0.5°,

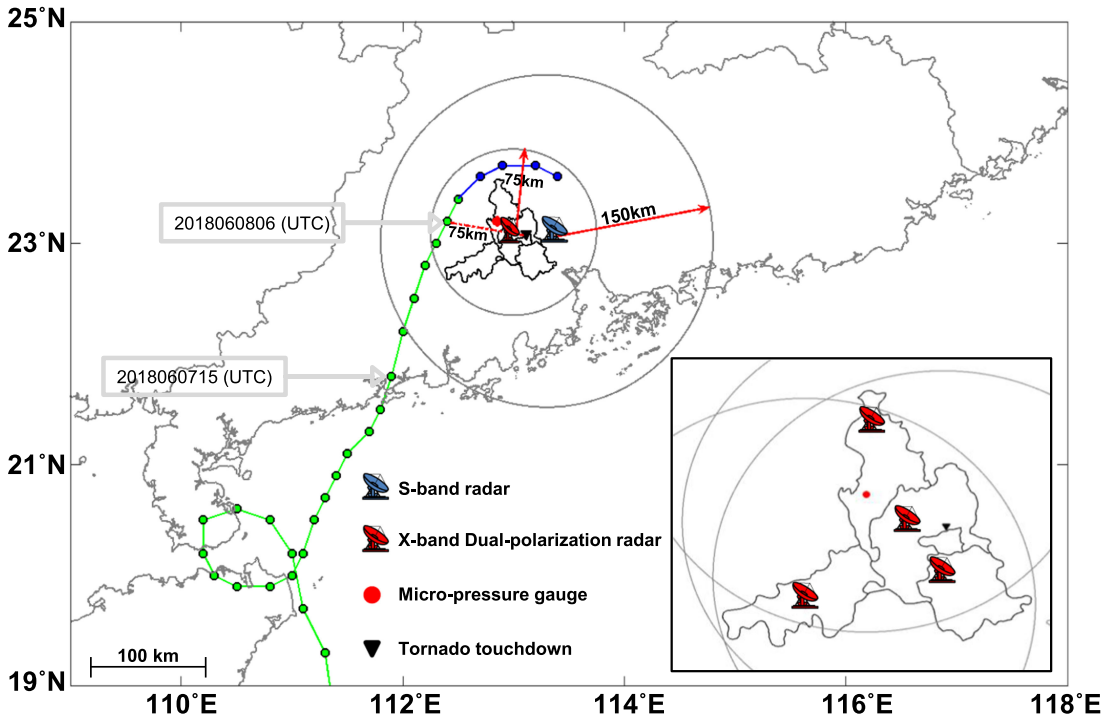

Fig. 2. TC track and distribution of observational instruments. The blue and green solid dots indicate the TC track at different stages (obtained from tcdata.typhoon.org.cn): blue solid dots are the TS stage, and green solid dots are the TD stage. The S-band Doppler radar has a detection range of 230 km, and the X-band dual-polarization radar detection range is 75 km. The red point indicates the location of the boundary layer wind-profiling radar and micropressure gauge. The inverted triangle represents the tornado touchdown, which occurred in the TS stage at a distance of approximately 75 km from the TS location at 06:00 UTC on June 8. The subfigure in the higher right corner is the X-band radar network with a coverage range of 75 km.

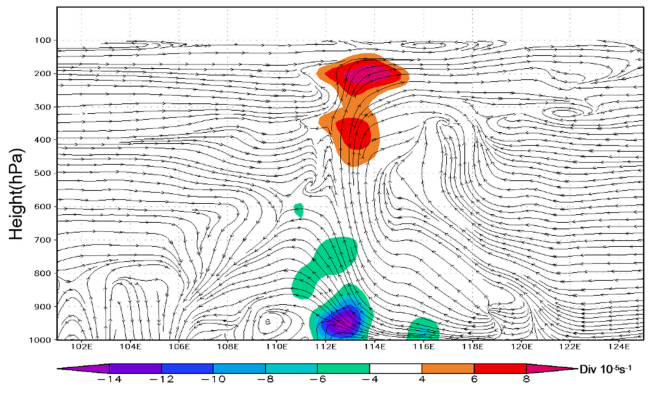

Fig. 3. Vertical cross section of divergence and updraft movements and wind speed.

1.4°, 2.4°, 3.3°, 4.3°, 6°, 9.9°, 14.6°, and 19.5°. The update rate of the S-band is approximately 6 min.

The tornado touchdown was located at an azimuth angle of 108.5°, approximately 13.2 km from the radar. In this VCP model, the direct detection heights were approximately 530 and 760 m at the 1.8° and 2.8° elevation angles, respectively.

The micropressure gauge is composed of a thermostat-controlled cavity, inner intelligent pressure sensor, and an external temperature indicator. The barometric pressure data were recorded at a sampling frequency of 1 Hz with a resolution of 0.1 Pa and a measurement error of 1 Pa; eventually, the high-precision dataset on the second scale was recorded in real time. An intelligent pressure sensor is the key component of this device [43] with a working environment temperature of $45° \pm 1°$, which is supplied by a thermostat-controlled cavity. The periods and amplitudes in the frequency domain of GWs hide in the barometric pressure data in the time domain. The dynamic spectrum characteristics of periods and amplitudes are extracted through a fast Fourier transform (FFT) at a fixed sampling time, which has myriad effects and major contributions to the circulation, structure, and variability in the atmosphere.

The X-band radar polarization parameters of Z_{DR} and ρ_{HV} were corrected using the methods presented by Ryzhkov *et al.* [19], and ϕ_{DP} was processed by linear programming. The related equations are shown as follows:

$$Z_{\mathrm{DR}}(\theta) \approx \frac{Z_{\mathrm{DR}}(0)}{[Z_{\mathrm{DR}}(0)^{1/2}\sin^2(\theta) + \cos^2(\theta)]^2} \tag{1}$$

$$\rho_{\mathrm{HV}}^{\mathrm{Cor}} = \rho_{\mathrm{HV}} \times (1 + 1/\mathrm{SNR}) \tag{2}$$

where $Z_{\mathrm{DR}}(0)$ and $Z_{\mathrm{DR}}(\theta)$ are differential reflectivities at elevation angles 0 and θ, respectively. SNR is the signal-to-noise ratio.

III. Synoptic Conditions

TC Ewiniar was generated on the southern surface of the South China Sea at 06:00 UTC on June 2 and landed three times throughout the entire process. At 00:00 UTC on June 8, the Pearl River Delta region was located in the strong south-southeast

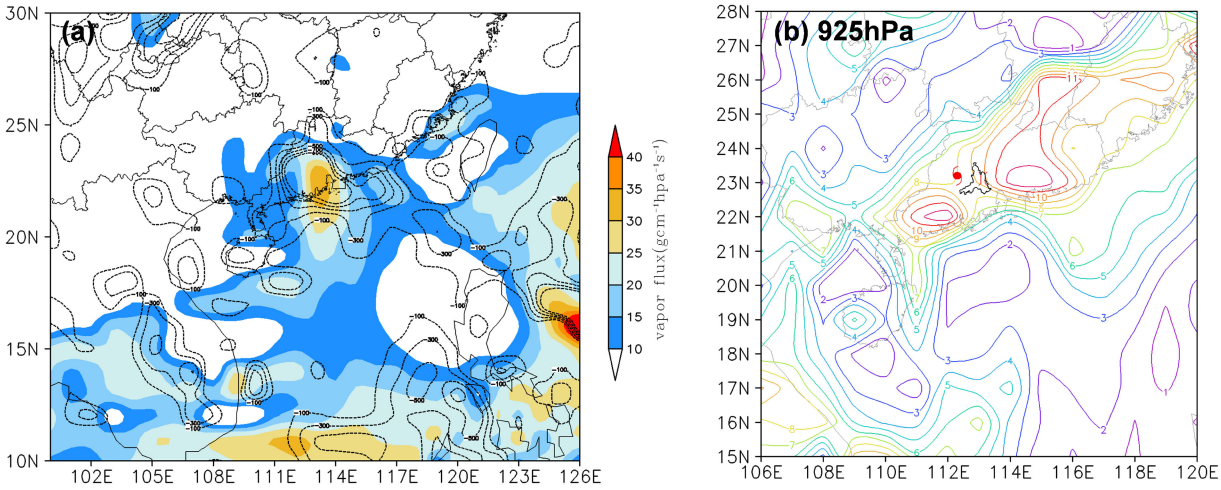

Fig. 4. (a) Water vapor flux (solid color lines) and water vapor flux divergence (isotherms), and (b) vertical wind shear at 06:00 UTC.

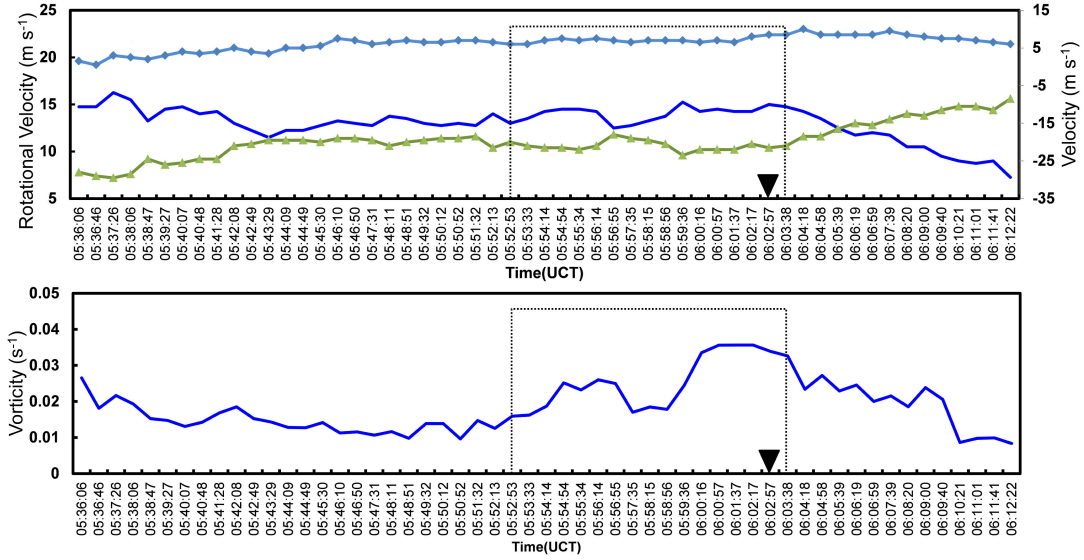

Fig. 5. (a) Evolution of the rotational velocity (blue line) and Doppler velocity (dark blue line is positive Doppler velocity, whereas green line is negative Doppler velocity). (b) Vorticity during the tornado storm event.

(SSE) jet stream core between the high-pressure circulation and the Ewiniar cyclone. The lower level of the Pearl River Delta region was located in the strong convergence zone of the southerly to southeast jet, and the southeast wind speeds at 925 and 850 hPa were 14 and 16 m/s, respectively, while the southerly wind speeds at 700 and 500 hPa increased to 20 and 18 m/s, respectively. A high level at 200 hPa with a divergence signature was also observed near the Pearl River Delta region. The vertical cross section of the divergence and updraft movements and wind speed in Fig. 3 depicts the favorable configuration of low-level convergence and high-level divergence. The height of convergence extends up to 600 hPa, the divergence value of the low-level convergence center reaches $-14.0 \times 10^{-5}\mathrm{s}^{-1}$, and the whole layer shows strong upward movement. The moisture flux divergence and vertical wind shear (VWS) at 925 hPa at 06:00 UTC are shown in Fig. 4. Therefore, the strong convergence of the middle- and low-level SSE jet stream and powerful upward movement provided a favorable large-scale background to trigger and organize tornadic convective storms.

The synoptic situation of upper-level divergence, low-level convergence, and superimposition of strong southeasterly jets at mid- and low-layers over the Pearl River Delta are conducive to the background weather of tornadoes. The common environmental conditions for tornado genesis appear to be a low lifting condensation level (LCL) ($\leq$1000 m), strong deep layer, and low-level VWS (greater than 10 m/s at 0–1 km and greater than 15 m/s at 0–6 km) and a high storm relative helicity (SHR; $\geq 100\ \mathrm{m}^2\ \mathrm{s}^{-2}$).

A data analysis from the Qingyuan radiosonde station, which has a distance of 70 km from Nanhai District, showed that the entire layer of 1000–500 hPa had low temperatures, small

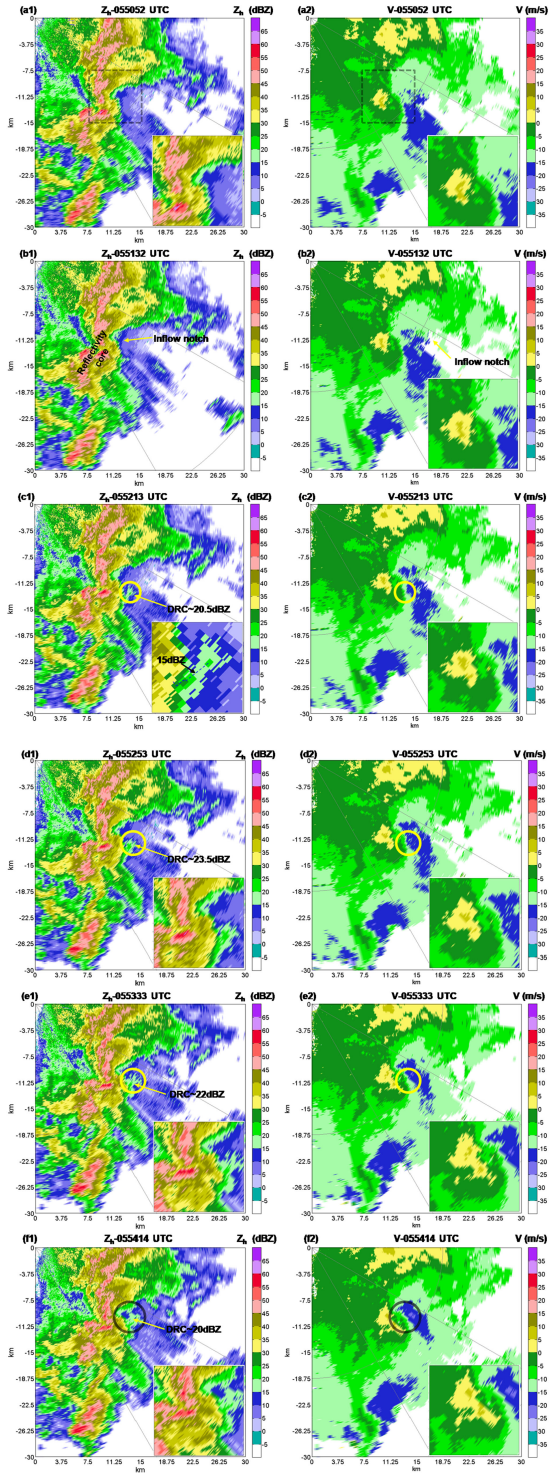

Fig. 6. Evolution of the DRC pattern from 05:50:22 to 05:54:14 UTC: (left) PPI scans of reflectivity and (right) Doppler velocity at elevation angle of 1.8°. The marked circles indicate the DRC area.

dew point differences, and low LCLs close to the ground, as well as a warm and humid atmosphere with a deep wet layer. Due to continuous heavy rainfall, unstable energy was partially released, and the convective available potential energy (CAPE) decreased from 750 J/kg at 12:00 UTC on the 7th to 138 J/kg at 00:00 UTC on the 8th, indicating that the atmospheric instability was weak at this time. However, the Hong Kong radiosonde station in the upstream direction had a high CAPE of 1327 and 1694 J/kg at 12:00 UTC on the 7th and at 00:00 UTC on the 8th before the occurrence of the tornado, supplying water vapor and heating the tornado area through the low-level southeast wind and providing favorable thermal and water vapor conditions for maintaining a certain amount of CAPE.

The atmospheric environmental parameters of strong low-level VWS and SRH represent significant changes conducive to the occurrence of tornadoes. The low-level VWS of 0–1 km increased from $9.9 \times 10^{-3}\mathrm{s}^{-1}$ at 12:00 UTC on the 7th to $11.3 \times 10^{-3}\mathrm{s}^{-1}$ at 00:00 UTC on the 8th, while the SRH enlarged from 142 $\mathrm{m}^2\mathrm{s}^2$ at 12:00 UTC on the 7th to 215 $\mathrm{m}^2\mathrm{s}^2$ at 00:00 UTC on the 8th. The strong low-level vertical shear and higher SHR provided favorable dynamic conditions for triggering strong convective storms.

IV. Multivariate Features of the Tornado

Based on the data obtained from the observational instruments, the vertical vorticity (V_{vor}) along with the rotational velocity (V_{rot}) were analyzed to resolve the mesocyclone features of the tornado evolution. Polarization characteristics, including the DRC pattern, Z_{DR} arc and K_{DP} foot signatures, and the separation of the Z_{DR} arc and K_{DP} foot, were investigated at different phases of the tornado. The periods and amplitudes of the GWs during this tornado were demonstrated in the three-dimensional dynamic spectrum.

A. X-Band Polarimetric Radar Observations: Tornadic Signatures

Minute-scale data from the X-band polarimetric radar were collected from 05:36 to 06:14 UTC, including Z_h, V, SW, and the polarimetric observables Z_{DR}, ρ_{HV}, and K_{DP}.

1) Mesocyclone Identification: A mesocyclone was developed prior to the tornado formation. Fig. 5 shows the evolution of V_{rot} and V_{vor}, which were calculated from the maximum and minimum velocities in the velocity couplet based on the following equations:

$$V_{\mathrm{rot}} = \frac{V_{\mathrm{max}} - V_{\mathrm{min}}}{2} \tag{3}$$

$$V_{\mathrm{vor}} = \frac{2(V_{\mathrm{max}} - V_{\mathrm{min}})}{D} \tag{4}$$

where V_{max} is the maximum velocity, V_{min} is the minimum velocity, and D is the distance between the location of V_{max} and V_{min}. Generally, V_{vor} should be greater than 0.01 s^{-1} during a mesocyclone [44]–[46]. This is also confirmed by Fig. 5 during this tornado event. As shown in Fig. 5(b), the location of the inverted triangle shows the time of tornado touchdown at 06:03 UTC, and the vorticity was mostly consistent at approximately 0.015 s^{-1} from 05:36 to 05:51 UTC. From 05:52 UTC, the vorticity showed an increasing trend, climbing up to a peak value of 0.026 s^{-1} at 05:56 UTC. Between 05:57 and 05:59 UTC, the vorticity dropped to 0.018 s^{-1} and then increased rapidly to the maximum of 0.035 s^{-1} at 06:01 UTC, 2 min before the tornado

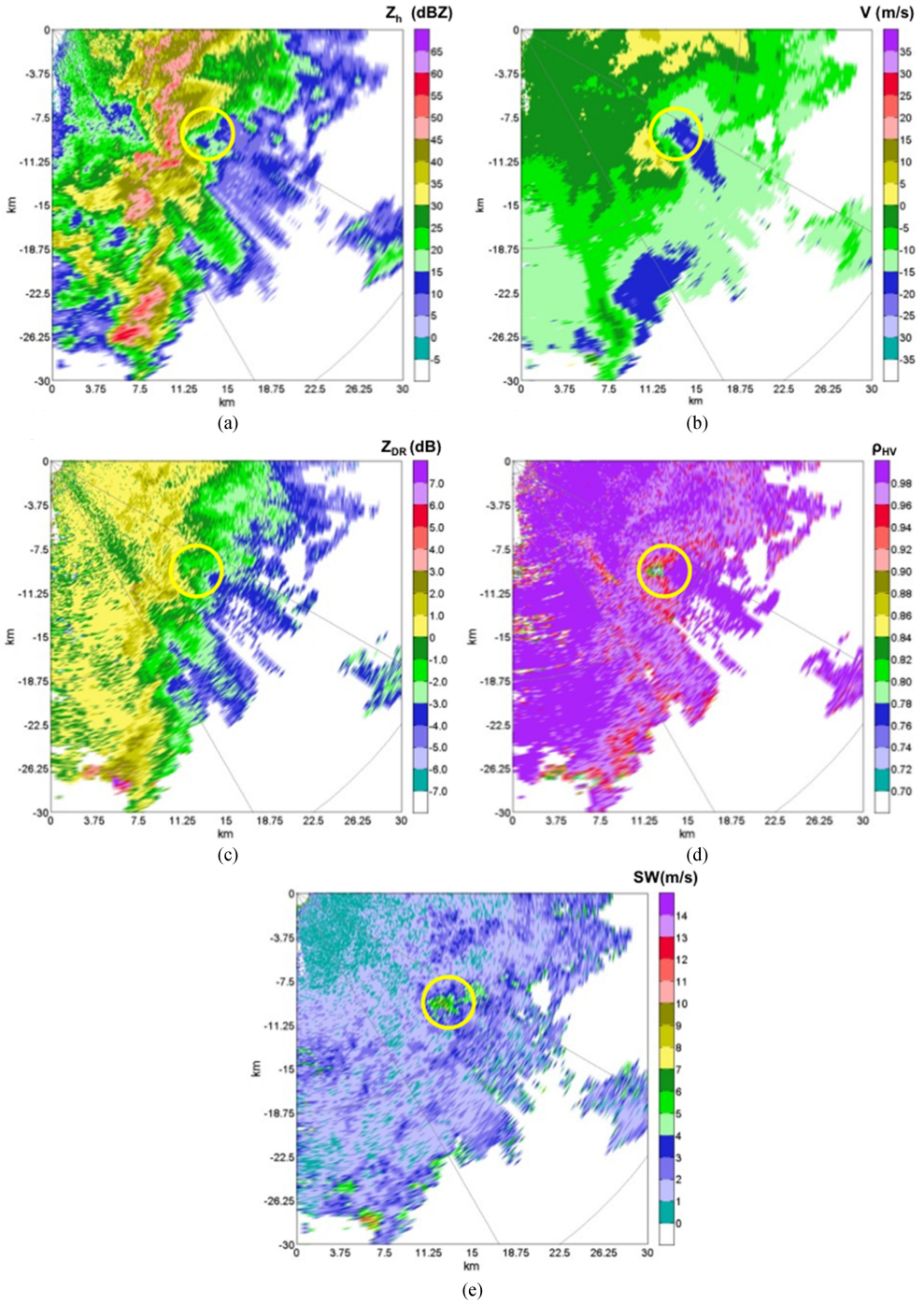

Fig. 7. PPI scans of (a) reflectivity, (b) Doppler velocity, (c) differential reflectivity, (d) co-polar correlation coefficient, and (e) SW at 05:54:14 UTC. The marked yellow circle means the same position of ρ_{HV} and Z_{DR} corresponding to the hook echo region and the center position of velocity couplet.

touched down. After 06:04 UTC, a decreasing vorticity trend was observed, demonstrating the dissipation of the tornado. This evolution feature can also be reflected by the V_{rot} field shown in Fig. 5(a), which reveals a smoothing trend between 05:36 and 06:03 UTC with an average value of 13.7 ms^{-1}. The emergence of positive Doppler velocities began at 05:36 in the left direction of the moving echo, and a velocity couplet formed. The mean value was maintained at approximately 5.7 ms^{-1} as affected by the environmental wind field. The mesocyclone appeared at 05:54 UTC, which was also observed by the S-band Doppler radar. After 06:04 UTC, the rotational velocity concussively decreased, and the mesocyclone weakened to shear.

2) DRC Pattern: The concept of the DRC was first proposed by Rasmussen *et al.* [15] and is essentially an isolated echo similar to a blob pendant from the rear side of the main radar echo. As suggested by Rasmussen *et al.* [15], some DRCs can be linked to the velocity couplet and provide a direct indication of tornado genesis. Kennedy *et al.* [16] collected

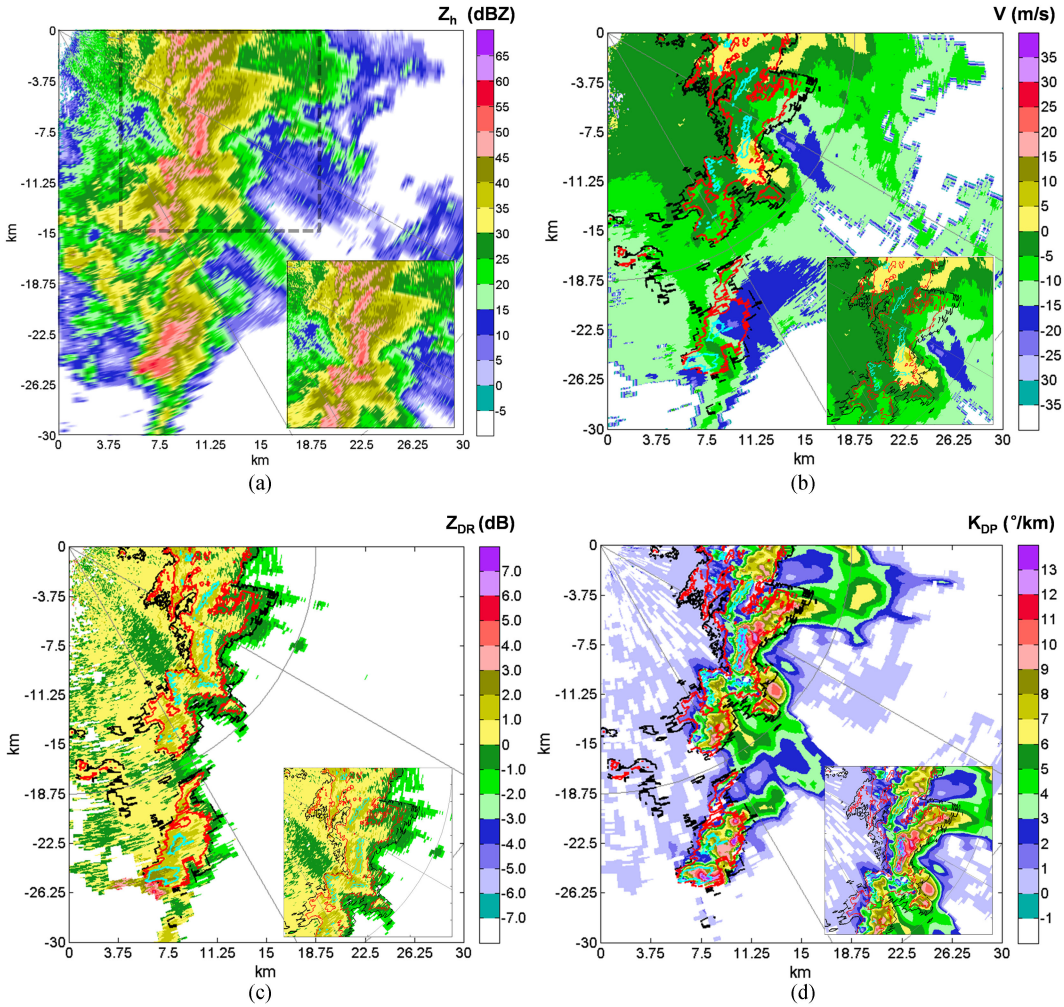

Fig. 8. 1.8° PPI scans of (a) reflectivity (Z_h; dBZ), (b) Doppler velocity (V; m/s), (c) differential reflectivity (Z_{DR}; dB), (d) specific differential phase (K_{DP}; °/km) at 05:55:34 UTC on June 8, 2018. Contours of Z_h (dBZ; 30, black line, 40, red line, and 50, blue line) are overlaid on each of the panels. The subfigures in the lower right corners indicate a zoomed-in area ($X = 3.75$ to 18.75 km, $Y = 0$ to –15 km).

a large number of DRC cases during 64 isolated supercells, and they concluded that 59% of the supercells generated DRCs and 30% of the generated DRCs were sustained for 15 min, approximately 10 min ahead and 5 min behind the tornado genesis. In this study, high spatiotemporal resolution X-band data were utilized to probe the DRC phenomenon with a short distance of 13 km away from the radar. The evolution process of the DRC is demonstrated in Fig. 6. The initial phase of the hook echo at 05:50:52 UTC is shown in Fig. 6(a), when there is no apparent DRC feature. At 05:51:32 UTC, an isolated echo with a maximum reflectivity of 17.5 dBZ appeared at the rear right of the main storm echo, exhibiting a dot-like echo separated from the main echo. In addition, the isolated echo was associated with a wide range of Doppler velocity spinning areas near the distinct inflow notch shown in Fig. 6(b2). The maximum reflectivity echo reached 20 dBZ with a distance of approximately 2.0 km from the main echo at 05:52:13 UTC [Fig. 6(c)]. At 05:52:53 UTC, the area of DRC expanded, and the maximum reflectivity was 23.5 dBZ, the highest measured reflectivity throughout the DRC phenomenon [Fig. 6(d)]. From 05:53:33 UTC to 05:54:14 UTC, the maximum reflectivity was stable at approximately 20 dBZ, and a velocity couplet appeared in the Doppler velocity at the corresponding location, as illustrated in Fig. 6(f). This phenomenon disappeared in the next two volume scans. Here, it should be noted that the corresponding vertical structure (i.e., RHI scans) was not fully captured by the X-band dual-polarization radar since only two low-level scans were conducted (i.e., 1.8° and 2.8° scans). S-band Doppler radar was utilized to supplement the observations of the vertical structure of the detected DRC, which will be detailed in Section IV-B. As explained, the apparent hook echo, mesocyclone exit, distinct inflow notch, and horizontal scale of approximately 30 km are attributes of mini-supercells embedded within rain shields.

3) Z_{DR} Arc and K_{DP} Foot Signatures and Their Separation: Simultaneously, the features of ρ_{HV} and Z_{DR} corresponding to the hook echo region and the center position of the velocity couplet were present at 05:54:14 UTC, as shown in Fig. 7. The horizontal range of this region was approximately 1.5 km. The mean Z_{DR} and ρ_{HV} values were approximately 0.5 dB and 0.73, respectively, and the spectrum width had large values

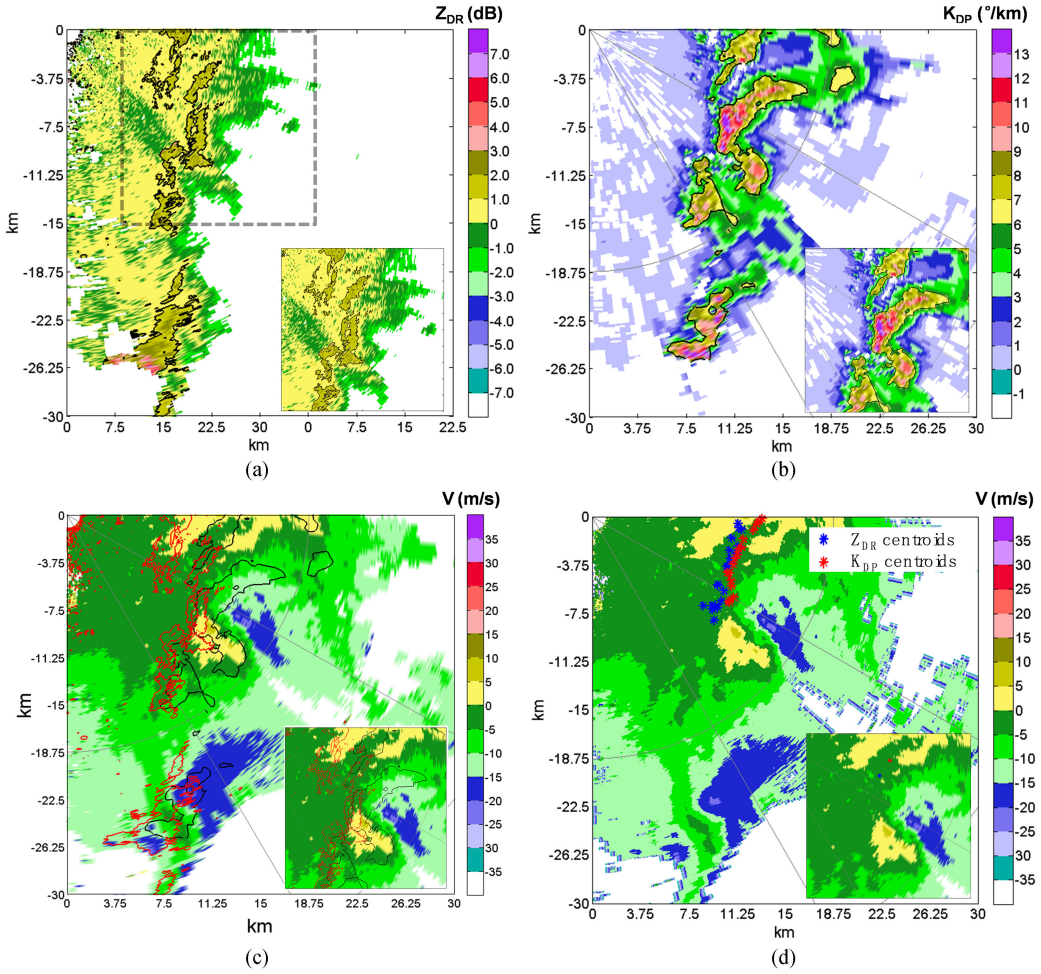

Fig. 9. 1.8° PPI scans at 05:55:34 UTC on June 8, 2018. (a) Differential reflectivity (Z_{DR}; dB) with contours of 1.5 dB. (b) Specific differential phase (K_{DP}; °/km) with contours of 6 dB. (c) Contours of Z_{DR} (dB; 1.5, red line) and K_{DP} (°/km; 6, black line) overlaid on Doppler velocity. (d) Z_{DR} and K_{DP} centroids from 05:48:51 to 06:14:22 UTC, blue (red) asterisks indicate the location of the Z_{DR} (K_{DP}) centroids overlaid on Doppler velocity. The subfigures in the lower right corners indicate a zoomed-in area ($X = 3.75$ to 18.75 km, $Y = 0$ to –15 km).

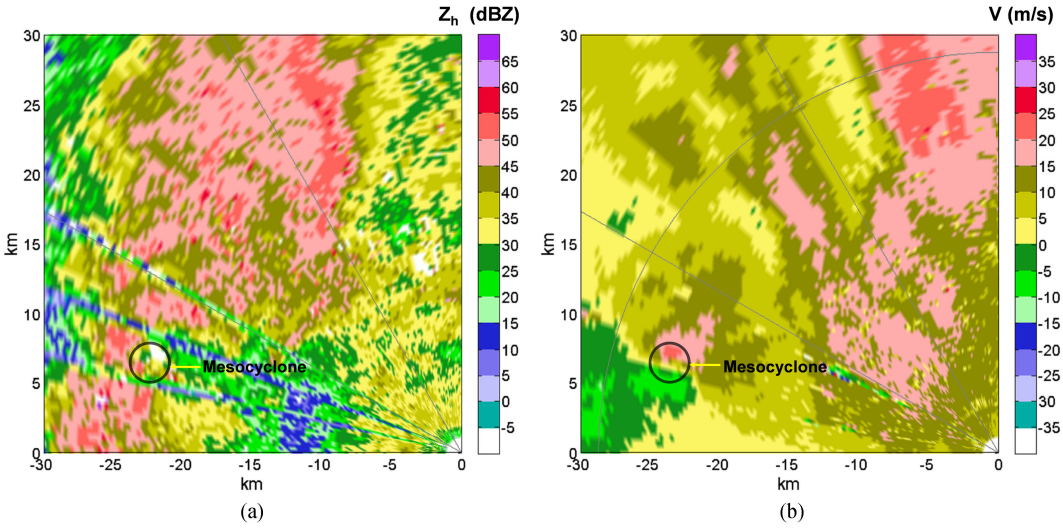

Fig. 10. (a) Radar reflectivity and (b) Doppler velocity at 1.5° elevation angle from the S-band Doppler radar at 05:54 UTC. Mesocyclone (black circle) was automatically identified.

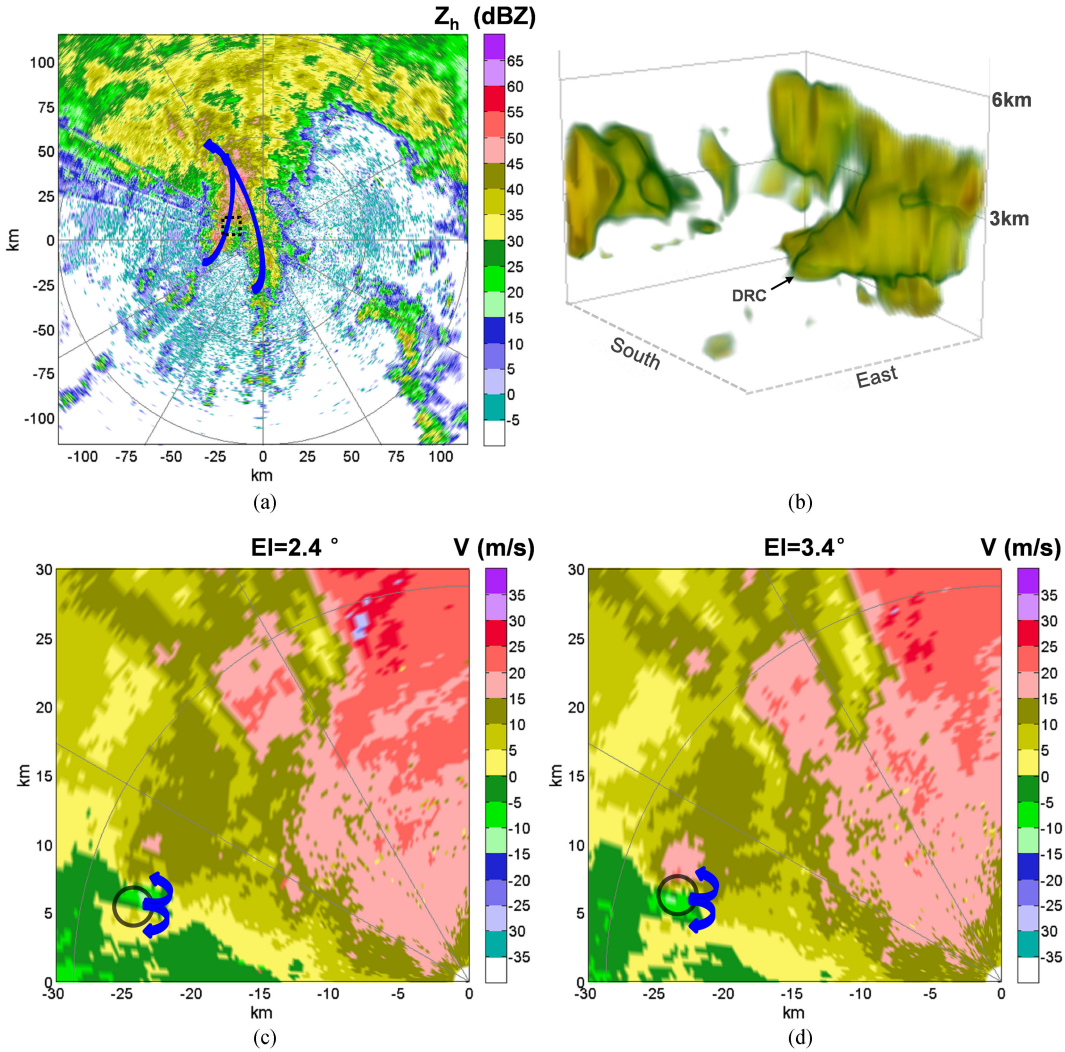

Fig. 11. (a) Two spiral rainbands converge as indicated by the blue arrows. (b) Three-dimensional perspective view of the 30-dBZ isosurface prior to tornado formation. The descending reflectivity core is marked DRC. (c) and (d) Velocity couplet that consists of inbound and outbound velocities (counter-rotating velocity vortices) at 2.4° and 3.4° elevation angles, respectively.

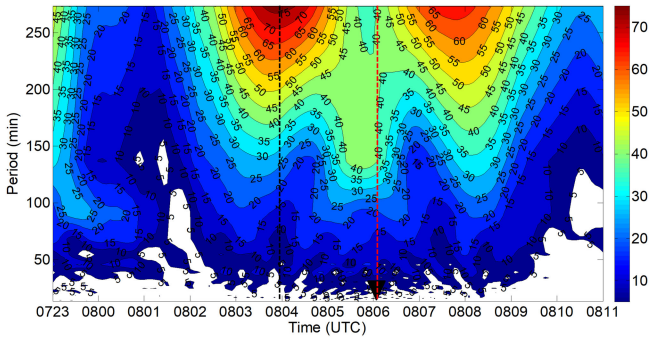

Fig. 12. Three-dimensional dynamic spectrum including periods and amplitudes of the GWs from 23:00 UTC on June 7 to 11:00 UTC on June 8, 2018. The black dotted line is the maximum amplitude fluctuation of the long period, and the red dotted line indicates the tornado touchdown.

greater than 5 ms^{-1}, indicating the existence of an area full of different hydrometeor particles and the existence of a strong updraft. The strong echo contours of Z_h (dBZ; 30, 40, 50) were overlaid on the polarimetric radar variables and Doppler velocity at 05:55:34 UTC in Fig. 8. An echo area with a value greater than 40 dBZ was centrally located at the left front of the supercell near the inflow notch. A Z_h contour greater than 50 dBZ was mainly distributed on the positive velocity region of the velocity couplet. The configuration between the strong echo, Z_{DR} and K_{DP} is thoroughly accounted for in Fig. 8(c) and (d), where high Z_{DR} values (>2 dB) are found along the higher Z_h gradient. The subfigures in the lower right corners indicate a zoomed-in area ($X = 3.75$ to 18.75 km, $Y = 0$ to –15 km).

Another obvious feature is the Z_{DR} arc and K_{DP} foot, as revealed in Fig. 9 at 05:55:34 UTC. The contours of Z_{DR} (1.5 dB) and K_{DP} (6°/km) displayed in Fig. 9(a) and (b) show the enhanced region associated with the supercell. Two focus regions need to be considered from Fig. 9(c). One is the region of K_{DP} distributed in front of the velocity couplet, which was sustained from 05:48:51 to 06:14:22 UTC (not shown). The values were greater than 6°/km with low Z_{DR} values, indicating

mixed-phase hydrometeors composed of melting hail; notably, K_{DP} is very sensitive to small melting hail. The other region is the separation between the enhanced Z_{DR} and K_{DP} along the inflow side of the FFD shown in Fig. 9(c), containing some overlapping area. The Z_{DR} arc and K_{DP} foot were extracted from 05:48:51 to 06:02:17 UTC taking into account ρ_{HV} values greater than 0.95 [47], whose centroids were calculated based on the method of Loeffler and Kumjian [27]. The separation distance was approximately 2.1 km shorter than the typical distance of 4 km described in [28].

B. S-Band Doppler Radar Observation: Tornadic Signatures

1) Mesocyclone Feature: The tornado parent convective storms moved to the Chancheng District at 05:42 UTC. The maximum reflectivity echo of 55 dBZ was present at a 0.5° elevation angle with a height of 0.5 km above ground level. A weak mesocyclone with a rotation speed of 12.0 m/s was detected at the corresponding location. At a 1.5° elevation angle, the rotation speed was up to 15 m/s with a height of 0.9 km, which is in line with the standard of a moderate-intensity mesocyclone. From 05:54 to 06:00 UTC, the tornado parent convective storms produced torrential rain and wind gusts in Dali Town, and the velocity couplet could be clearly observed at different lower elevations from 0.5° to 4.3°. At a 1.5° elevation angle, the mesocyclone continued to strengthen with a rotation speed of 16 m/s, and the horizontal distance between the maximum and minimum radial velocities in the velocity couplet was approximately 1.8 km. The mesocyclone was automatically identified by the S-band Doppler radar at 05:54 UTC, as shown in Fig. 10.

2) DRC Pattern: Two spiral rainbands converged to become one along the blue arrows shown in Fig. 11(a). Corresponding to the mesocyclone identified by the S-band Doppler radar, the three-dimensional isosurfaces of 30 dBZ reflectivity are shown in Fig. 11(b). The blob-like echo protuberance pendant off the main radar echo illustrates the presence of the DRC. The DRC was located at a height of approximately 1.5 km with a horizontal distance of approximately 500 m from the main echo. Moreover, the velocity couplet composed of inbound and outbound velocities (counter-rotating velocity vortices) at elevations of 2.4° and 3.4° is shown in Fig. 10(c) and (d). The DRC pattern prior to tornado formation may be caused by hydrometeors sinking from the tornado parent convective storms [48].

C. Second-Scale Micropressure Gauge Observations

The three-dimensional dynamic spectrum including the periods and amplitudes of the GWs over time on June 8, 2018, is shown in Fig. 12. The spectrum was calculated by FFT with 214 sampling points based on the microbarograph data every second. The amplitude fluctuation of the long period of 100–250 min was between 20 and 75 Pa, and the short period of 50–99 min was between 10 and 20 Pa. The amplitude fluctuation of the long period suddenly increased to 77.3 Pa at approximately 04:00 UTC, 2 h before the tornado occurred, which may be an early tornado signature that can be used for warning operations. When the tornado occurred at 06:03 UTC, the amplitude fluctuation of the long period was between 25 and 45 Pa, and the short period was between 5 and 20 Pa. The amplitude fluctuation was reduced by approximately 38.5 Pa.

V. Conclusion

An EF1 tornado associated with TC Ewiniar occurred in Dali Town, Guangdong Province, on June 8, 2018. The synoptic conditions, polarimetric radar characteristics, and GW features of this tornado were analyzed using multivariate observations. The vertical vorticity evolution indicates that the formation of the tornado was related to a mesocyclone, reaching a maximum of 0.035 s^{-1} before the tornado touchdown. The signatures of the DRC and its three-dimensional structure, the Doppler velocity couplet, Z_{DR} and K_{DP} arcs were thoroughly investigated. The location of the tornado touchdown was approximately 13.2 km from the X-band polarimetric radar and 24 km from the local S-band Doppler radar, both of which were able to detect the DRC at fine scales. The velocity couplet, which is considered the most obvious feature of a tornado, was observed by both radars, and the combination of X- and S-band observations can serve as an accurate indicator of tornado. Two focus regions with K_{DP} values greater than 6°/km are presented by combining the Doppler velocity couplet and Z_{DR} arc. The separation distance of the Z_{DR} arc and K_{DP} foot was approximately 2.1 km. The appearance of these features may be indicative of fundamental processes intrinsic to tornadic storms. In addition, the amplitude of the GWs of the tornado in the long period suddenly increased to 77.3 Pa, 2 h before the tornado occurred. It is concluded that the DRC, along with the velocity couplet, the GW characteristics, as well as the separation distance of the Z_{DR} arc and K_{DP} foot can be used for early warnings of tornadoes.

Since it is the first TC tornado that was captured by a high-resolution X-band dual-polarization radar, this article is expected to provide supplemental observations to the global severe weather community. Similar to the midlatitude tornado events reported in the literature, this tornado within a TC rainband is characterized by a low-value region of ρ_{HV}, indicating the potential of using this polarimetric variable to monitor tornadoes. Compared with the operational S-band radar, the X-band observations have a great advantage in identifying the tornado signatures due to its super high spatial resolution and rapid-scan strategy. A comprehensive analysis of the activity characteristics, synoptic and environmental situation, especially the radar-observed features of 16 cataloged tornadoes occurred during 11 typhoon events in Pearl River Delta is in progress [31]. Considering that the Pearl River Delta has been deploying a high-resolution X-band dual-polarization phased-array radar network, this study may provide a scientific reference for the future use of radar data.

In addition, this article summarized the typhoon track and the range of typhoon position prone to triggering tornadoes. The Tornado Disaster Monitoring System (TDMS) is configured through integrating such information. The Tornado Targeted Release System (TTRS) is developed to superimpose tornado early warning release tools and special highly sensitive power facilities and disaster-prone areas. Based on the TDMS and

TTRS systems, the tornado warning was successfully issued 58 min in advance. This specific tornado warning was the first ever in China and was critical to improving decision making during strong convective weather events. In the future, new monitoring tools such as X-band radars and adaptive scan strategies should be deployed at a larger scale to further enhance the monitoring and forecasting of short-lived extreme weather events.

REFERENCES

[1] M. Xue, K. Zhao, M. Wang, Z. Li, and Y. Zheng, "Recent significant tornadoes in China," *Adv. Atmos. Sci.*, vol. 33, no. 11, pp. 1209–1217, 2016.

[2] N. Dotzek, P. Groenemeijer, B. Feuerstein, and A. M. Holzer, "Overview of ESSL's severe convective storms research using the European severe weather database ESWD," *Atmos. Res.*, vol. 93, no. 1, pp. 575–586, 2009.

[3] W. J. Fan and X. D. Yu, "Characteristics of spatial-temporal distribution of tornadoes in China," *Meteorological Monthly*, vol. 41, no. 7, pp. 793–805, 2015.

[4] T. T. Fujita, "Structure and movement of a dry front," *Bull. Amer. Meteor. Soc*., vol. 39, pp. 574–582, 1958.

[5] T. Fujita, "Formation and steering mechanisms of tornado cyclones and associated Hook echoes," *Mon. Wea. Rev.*, vol. 93, pp. 67–78, 1965.

[6] K. A. Browning and R. J. Donaldson, "Airflow and structure of a tornadic storm," *J. Atmos. Sci*., vol. 20, pp. 533–545, 1963.

[7] K. A. Browning, "Airflow and precipitation trajectories within severe local storms which travel to the right of the winds," *J. Atmos. Sci.*, vol. 21, pp. 634–639, 1964.

[8] D. W. Burgess and R. A. Brown, "The structure of a severe right-moving thunderstorm: New single Doppler radar evidence," in *Proc. 8th Conf. Severe Local Storms*, Denver, CO, USA: American Meteorological Society, 1973, pp. 40–43.

[9] R. A. Brown, W. C. Bumgarner, K. C. Crawford, and D. Sirmans, "Preliminary Doppler velocity measurements in developing radar hook echo," *Bull. Amer. Meteor. Soc.*, vol. 52, pp. 1186–1188, 1971.

[10] D. W. Burgess, L. R. Lemon, and R. A. Brown, "Tornado characteristics revealed by Doppler radar," *Geophys. Res. Lett.*, vol. 2, pp. 183–184, 1975.

[11] R. A. Brown, L. R. Lemon, and D. W. Burgess, "Tornado detection by pulsed Doppler radar," *Mon. Wea. Rev.*, vol. 106, no. 1, pp. 29–38, Jan. 1978.

[12] E. N. Rasmussen *et al.*, "Overification of the origins of rotation in tornadoes experiment: Vrtex," *Bull. Amer. Meteo. Soc.*, vol. 75, no. 6, pp. 995–1006, 1994.

[13] R. M. Wakimoto, C.-H. Liu, and H. Cai, "The garden city, kansas, storm during VORTEX 95. Part I: Overview of the storm's life cycle and mesocyclogenesis," *Mon. Wea. Rev.*, vol. 126, pp. 372–392, 1998.

[14] J. Wurman *et al.*, "The second verification of the origins of rotation in tornadoes experiment: VORTEX2," *Bull. Amer. Meteor. Soc.*, vol. 93, pp. 1147–1170, 2012.

[15] E. N. Rasmussen, J. M. Straka, M. S. Gilmore, and R. Davies-Jones, "A preliminary survey of rear-flank descending reflectivity cores in supercell storms," *Wea. Forecasting*, vol. 21, pp. 923–938, 2006.

[16] A. D. Kennedy, J. M. Straka, and E. N. Rasmussen, "A statistical study of the association of DRCS with supercells and tornadoes," *Wea. Forecasting*, vol. 22, pp. 1192–1199, 2007.

[17] Z. Byko, P. Markowski, Y. Richardson, J. Wurman, and E. Adlerman, "Descending reflectivity cores in supercell thunderstorms observed by mobile radars and in a high-resolution numerical simulation," *Wea. Forecasting*, vol. 24, no. 1, pp. 155–186, Feb. 2009.

[18] A. V. Ryzhkov *et al.*, "Polarimetric analysis of a 3 May 1999 tornado," in *Proc. 21st Conf. Severe Local Storms*, San Antonio, TX, USA: American Meteorological Society, 2002, pp. 515–518.

[19] A. V. Ryzhkov, T. J. Schuur, D. W. Burgess, and D. S. Zrnic, "Polarimetric tornado detection," *J. Appl. Meteorol.*, vol. 44, pp. 557–570, 2005.

[20] H. B. Bluestein *et al.*, "Close-range observations of tornadoes in supercells made with a dual polarization, X-band, mobile Doppler radar," *Mon. Wea. Rev*., vol. 135, pp. 1522–1543, 2007.

[21] M. R. Kumjian and A. V. Ryzhkov, "Polarimetric signatures in supercell thunderstorms," *J. Appl. Meteorol. Climatol.*, vol. 47, pp. 194–1961, 2008.

[22] G. S. Romine, D. W. Burgess, and R. B. Wilhemson, "A dual-polarization-radar-based assessment of the 8 May 2003 Oklahoma city area tornadic supercell," *Mon. Wea. Rev.*, vol. 136, pp. 2849–2870, 2008. [Online]. Available: https://doi.org/10.1175/2008MWR2330.1

[23] J. C. Snyder, H. B. Bluestein, G. Zhang, and S. J. Frasier, "Attenuation correction and hydrometeor classification of high-resolution, xband, dual-polarized mobile radar measurements in severe convective storms," *J. Atmos. Ocean. Technol.*, vol. 27, pp. 1979–2001, 2010. [Online]. Available: https://doi.org/10.1175/ 2010JTECHA1356.1

[24] M. R. Kumjian and A. V. Ryzhkov, "The impact of size sorting on the polarimetric radar variables," *J. Atmos. Sci.*, vol. 69, pp. 2042–2060, 2012. [Online]. Available: https://doi.org/10.1175/JAS-D-11-0125.1

[25] C. C. Crowe, C. J. Schultz, M. Kumjian, L. D. Carey, and W. A. Petersen, "Use of dual-polarization signatures in diagnosing tornadic potential," *Electron. J. Oper. Meteorol.*, vol. 13, no. 5, pp. 57–78, 2012.

[26] S. M. Martinaitis, "Radar observations of tornado-warned convection associated with tropical cyclones over Florida," *Wea. Forecasting*, vol. 32, pp. 165–186, 2017. [Online]. Available: https://doi.org/10.1175/WAF-D-16-0105.1

[27] S. D. Loeffler and M. R. Kumjian, "Quantifying the separation of enhanced ZDR and KDP regions in nonsupercell tornadic storms," *Wea. Forecasting*, vol. 33, pp. 1143–1157, 2018.

[28] S. D. Loeffler, M. R. Kumjian, M. Jurewicz, and M. M. French, "Differentiating between tornadic and nontornadic supercells using polarimetric radar signatures of hydrometeor size sorting," *Geophys. Res. Lett.*, vol. 47, no. 12, 2020, Art. no. e 2020GL088242.

[29] R. M. Wakimoto *et al.*, "Photogrammetric analysis of the 2013 El reno tornado combined with mobile X-band polarimetric radar data," *Mon. Wea. Rev.*, vol. 143, pp. 2657–2683, 2015. [Online]. Available: https://doi.org/10.1175/MWR-D-15-0034.1

[30] Y. Zheng, X. D. Yu, and Q. B. Cai, "Analysis on a severe tornado process in Hainan triggered by supercell," (in Chinese), *Meteorol. Mon.*, vol. 43, pp. 675–685, 2017.

[31] X. Huang *et al.*, "Contrastive analysis of two intense typhoon-tornado cases with synoptic and Doppler weather radar data in Guangdong," *J. Appl. Meteorol. Sci*., vol. 29, no. 1, pp. 70–83, 2018.

[32] L. Bai, Z. Meng, K. Sueki, G. Chen, and R. Zhou, "Climatology of tropical cyclone tornadoes in China from 2006 to 2018," *Sci. China Earth Sci.*, vol. 63, pp. 37–51, 2020. [Online]. Available: https://doi.org/10.1007/s11430-019-9391-1

[33] Z. Y. Meng *et al.*, "The deadliest tornado (EF4) in the past 40 years in China," *Wea. Forecasting*, vol. 33, pp. 693–713, 2018.

[34] Y. G. Zheng, Y. Lan, and Y. C. Cao, "Environmental conditions, evolution and mechanisms of the EF4 tornado in Kaiyuan of Liaoning province on 3 July 2019," (in Chinese), *Meteorol. Mon.*, vol. 46, no. 5, pp. 589–602, 2020.

[35] L. Bai *et al.*, "An integrated damage, visual, and radar analysis of the 2015 Foshan, Guangdong, EF3 tornado in China produced by the landfalling typhoon Mujigae (2015)," *Bull. Amer. Meteor. Soc.*, vol. 98, no. 12, pp. 2619–2640, 2017.

[36] K. Zhao *et al.*, "Doppler radar analysis of a tornadic miniature supercell during the landfall of typhoon Mujigae (2015) in South China," *Bull. Amer. Meteor. Soc.*, vol. 98, pp. 1821–1831, 2017.

[37] Z. Li *et al.*, "Monitoring wildfire using high-resolution compact X-band dual-polarization radar: A case study in southern China," *Atmos. Res.*, vol. 225, pp. 165–171, 2019.

[38] H. Chen and V. Chandrasekar, "The quantitative precipitation estimation system for Dallas–Fort worth (DFW) urban remote sensing network," *J. Hydrol.*, vol. 531, pp. 259–271, 2015.

[39] H. Chen, S. Lim, V. Chandrasekar, and B.-J. Jang, "Urban hydrological applications of dual-polarization X-band radar: Case study in Korea," *J. Hydrologic Eng.*, vol. 22, no. 5, 2017, Art. no. E 5016001.

[40] V. Chandrasekar, H. Chen, and B. Philips, "Principles of high-resolution radar network for hazard mitigation and disaster management in an urban environment," *J. Meteorol. Soc. Jpn.*, vol. 96A, pp. 119–139, 2018.

[41] Y. W. Zhang *et al.*, "An overview of the China meteorological administration tropical cyclone database," *J. Atmos. Ocean. Technol.*, vol. 31, pp. 287–301, 2014.

[42] H. Yu *et al.*, "Western North Pacific tropical cyclone database created by the China meteorological administration," *Adv. Atmos. Sci.*, vol. 38, no. 4, pp. 690–699, 2021.

[43] F. Einaudi, L. W. Clark, and D. Fua, "Gravity waves and convection in colorado during July 1983," *J. Atmos. Sci.*, vol. 44, no. 11, pp. 1534–1553, 1987.

[44] O. Suzuki, H. Niino, H. Ohno, and H. Nirasawa, "Tornado producing mini supercells associated with typhoon 9019," *Mon. Wea. Rev.*, vol. 128, pp. 1868–1882, 2000.
[45] R. J. Donaldson, "Vortex signature recognition by a Doppler radar," *J. Appl. Meteorol.*, vol. 9, pp. 661–670, 1970.
[46] R. R. Lee and A. White, "Improvement of the WSR-88D mesocyclone algorithm," *Wea. Forecasting*, vol. 13, pp. 341–351, 1998.
[47] M. M. French, H. B. Bluestein, I. PopStefanija, C. A. Baldi, and R. T. Bluth, "Mobile, phased-array, Doppler radar observations of tornadoes at X band," *Mon. Wea. Rev.*, vol. 142, pp. 1010–1036, 2014.
[48] S. Lim, S. Allabakash, B. Jang, and V. Chandrasekar, "Polarimetric radar signatures of a rare tornado event over South Korea," *J. Atmos. Ocean. Technol.*, vol. 35, no. 10, pp. 1977–1997, 2018.

Zhaoming Li received the B.S. degree in signal and information processing from Chengdu University of Information Technology, Chengdu, China, in 2010, and the Ph.D. degree in atmospheric physics and atmospheric environment from Institute of Atmospheric Physics (IAP), Chinese Academy of Sciences, Beijing, China, in 2014.

He was with IAP as a Postdoc Researcher during 2014 and 2016. Since 2016, he has been a Radar Engineer and a Weather Forecaster with Foshan Tornado Research Center, Foshan, China. His research interests include collaborative adaptive sensing of weather radars, multivariate observation of severe convective storms, and tornado nowcasting.

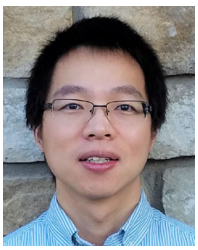

Haonan Chen (Senior Member, IEEE) received the Ph.D. degree in electrical engineering from Colorado State University (CSU), Fort Collins, CO, USA, in 2017.

He is currently an Assistant Professor with CSU. He worked with the NOAA Physical Sciences Laboratory, Boulder, CO, USA, from 2012 to 2020, first as a Research Student and then as a National Research Council Research Associate and a Radar, Satellite, and Precipitation Research Scientist. His research interest lies primarily in remote sensing and multidisciplinary data sciences, including radar and satellite observations of natural disasters, polarimetric radar systems and networking, Big Data analytics, multiscale hydrometeorological data fusion, and precipitation classification, estimation, and prediction using deep learning techniques.

Dr. Chen serves as an Associate Editor for the *Journal of Atmospheric and Oceanic Technology*, *URSI Radio Science Bulletin*, and *IEEE Journal of Selected Topics in Applied Earth Observation and Remote Sensing*.

Hongxing Chu photograph and biography not available at the time of publication.

Haobo Tan received the B.S. degree in atmospheric physics and atmospheric environment from Sun Yat-sen University, Guangzhou, China, in 2005, and the Ph.D. degree in atmospheric physics and atmospheric environment from Nanjing University of Information Science and Technology, Nanjing, China, in 2017.

He was with the Guangzhou Institute of Tropical Marine and Meteorology, China Meteorological Administration, Beijing, China, during 2005 and 2015, and with Guangdong Ecological Meteorology Center, Guangdong, China, during 2015 and 2019. He has been the Director of Foshan Meteorology Service, Foshan, China, since 2019. His research interests include physical and chemical characteristics of atmospheric aerosol, air pollution, radar observation of severe convective storms, cloud microphysics, and nowcasting.

V. Chandrasekar (Fellow, IEEE) received the bachelor's degree from IIT Kharagpur, Kharagpur, India, in 1981, and the Ph.D. degree from Colorado State University (CSU), Fort Collins, CO, USA, in 1986, all in electrical engineering.

He is currently a University Distinguished Professor with CSU. He has been a Visiting Professor with the National Research Council of Italy, Rome, Italy; the University of Helsinki, Helsinki, Finland; the Finnish Meteorological Institute, Helsinki, Finland; Tsinghua University, Beijing, China; and IIT Kharagpur and an Affiliate Scientist with the NASA Jet propulsion Laboratory, Pasadena, CA, USA. He is a Distinguished Visiting Scientist with the NASA Goddard Space Flight Center, Greenbelt, MD, USA, and a Distinguished Professor of Finland (FiDiPro). He has been the Director of the Research Experiences for Undergraduate Program, for over 25 years, promoting research in the undergraduate curriculum. He is also the Associate Dean of the College of Engineering for promoting international research collaboration. He has been actively involved with the research and development of weather radar systems for more than 35 years. He has played a key role in developing the CSU-CHILL National Radar Facility as one of the most advanced meteorological radar systems available for research and continues to work actively with the CSU-CHILL radar, supporting its research and education mission. He is also the Research Director of the National Science Foundation Engineering Research Center for Collaborative Adaptive Sensing of the Atmosphere. He is an avid experimentalist conducting special experiments to collect *in situ* observations to verify the new techniques and technologies. He is an author of two text books and five general books and more than 300 peer reviewed journal articles. He has served as an Academic Advisor for more than 70 graduate students.

Dr. Chandrasekar is a Fellow of the American Meteorological Society, American Geophysical Union, URSI, the National Oceanic and Atmospheric Administration (NOAA) Cooperative Institute for Research in the Atmosphere (CIRA), and the National Academy of Inventors. He has served as a Member for the National Academy of Sciences Committee that wrote the books *Weather Radar Technology Beyond NEXRAD* and *Flash Flood Forecasting in Complex Terrain*. He was a recipient of numerous awards, including Knighted by the Government of Finland, the NASA Technical Contribution Award, the NASA Group Achievement Award, the NASA Robert H. Goddard Exceptional Achievement Award, the Outstanding Advisor Award, the CSU Innovations Award, the IEEE GRSS Education Award, the NOAA/NWS Directors Medal of Excellence, and the IEEE GRSS Distinguished Achievement Award. He has served as the General Chair for the IEEE IGARSS'06 Symposium. He serves as the Chair for the Commission F, International Union of Radio Science (URSI). He also served as the Chief Editor for the *Journal of Atmospheric and Oceanic Technology*, an Associate Editor for IEEE TRANSACTIONS ON GEOSCIENCE AND REMOTE SENSING, and a Guest Editor for *IEEE Journal of Selected Topics in Applied Earth Observations and Remote Sensing*.

Xianxiang Huang photograph and biography not available at the time of publication.

Shuofu Wang photograph and biography not available at the time of publication.